Title

Hydro-mechanical modeling of the first and second hydraulic stimulations in a fractured geothermal reservoir in Pohang, South Korea

Authors

Yoo, Hwajung

Park, Sehyeok

Xie, Linmao

et al.

Publication Date

2021

DOI

10.1016/j.geothermics.2020.101982

Peer reviewed

Geothermics 89 (2021) 101982

Contents lists available at ScienceDirect

Geothermics

journal homepage: www.elsevier.com/locate/geothermics

Hydro-mechanical modeling of the first and second hydraulic stimulations in a fractured geothermal reservoir in Pohang, South Korea

Hwajung Yoo [a], Sehyeok Park [a], Linmao Xie [a], Kwang-Il Kim [a], Ki-Bok Min [a,*], Jonny Rutqvist [b], Antonio Pio Rinaldi [b,c]

[a] Department of Energy Systems Engineering, Seoul National University, 1, Gwanak-ro, Gwanak-gu, Seoul, 08826, Republic of Korea
[b] Lawrence Berkeley National Laboratory, 1 Cyclotron Rd, Berkeley, CA 94720, USA
[c] Swiss Seismological Service, Swiss Federal Institute of Technology, ETHZ, Sonneggstrasse 5, Zürich, 8092, Switzerland

ARTICLE INFO

Keywords:
Pohang EGS project
Hydraulic stimulation
Hydro-mechanical modeling
Hydraulic shearing
Hydraulic jacking
Pressure history matching

ABSTRACT

This study presents comprehensive coupled hydro-mechanical numerical modeling of the first and second hydraulic stimulations at the Pohang enhanced geothermal system (EGS) site in order to improve the understanding on the key stimulation mechanisms in the fractured reservoir. Two models for PX-2 and PX-1 wells were developed including fracture zones of different orientations and permeability. Shear dilation and frictional plastic strain-softening were implemented in a non-linear stress dependent fracture model. A history matching of the wellhead pressure curves was carried out in the early days of each stimulation. The PX-2 model with a fracture jacking mechanism achieved the reproduction of highly reversible non-linear aperture changes observed in situ. The PX-1 model successfully simulated a wellhead pressure peak and drop associated with shear slip and dilation by applying frictional plastic strain softening. Simulated critical wellhead pressure for shear slip near the PX-1 well was greater than the prediction by a simple slip potential analysis due to local stress changes by the poroelastic effect. The numerical modeling confirmed that the combination of shear dilation and jacking was adequate to capture the pressure evolution during the increasing step-rate test at PX-1. Besides, spatio-temporal changes in pressure, total stress, and permeability evaluated in the fracture zones greatly enhanced the understanding on the coupled behavior caused by the hydraulic stimulations. The possibility of zones with lower permeability away from the PX-1 well was suggested by an alternative model. The current numerical study demonstrates that the key hydro-mechanical processes of shear slip and dilation and hydraulic jacking observed in the fractured reservoir can be successfully reproduced.

1. Introduction

An enhanced geothermal system (EGS) aims to increase the permeability of the reservoir through hydraulic stimulation and make the flow path between the wells sufficiently permeable for commercial energy production rates. While pre-existing fractures can provide potential flow paths between the injection and production wells, reactivation of such fractures by hydraulic shearing is a key process for achieving a permanent increase in permeability by the dilation of fractures (Pine and Batchelor, 1984; Cladouhos et al., 2009). Hydraulic stimulation can also increase the permeability of a geothermal reservoir by creating new tensile fractures (Economides and Nolte, 2000) or reopening (or hydraulic jacking) of pre-existing fractures in tensile modes (Rutqvist and Stephansson, 1996). During reopening or closure of an existing fracture, it has been recognized that non-linear changes in fracture apertures with respect to effective normal stress have to be considered (Rutqvist and Tsang, 2003; Min et al., 2004). The abovementioned hydro-mechanical processes can often occur simultaneously including crack propagation, making it necessary to carry out comprehensive analysis on the underlying stimulation mechanisms (McClure and Horne, 2014; Kamali and Ghassemi, 2018; Norbeck et al., 2018).

Numerical modeling of hydraulic stimulations can improve the understanding on the mechanisms of reservoir permeability enhancement through history matching of flow-pressure curves with an appropriate conceptual model. Numerical simulations can be used to estimate the spatial and temporal changes in permeability during the stimulation and relationship between microseismicity and hydraulic stimulation. In addition, the properties of fractures such as stiffness, aperture, and

* Corresponding author.
E-mail address: kbmin@snu.ac.kr (K.-B. Min).

https://doi.org/10.1016/j.geothermics.2020.101982
Received 30 November 2019; Received in revised form 29 August 2020; Accepted 8 October 2020
Available online 17 October 2020

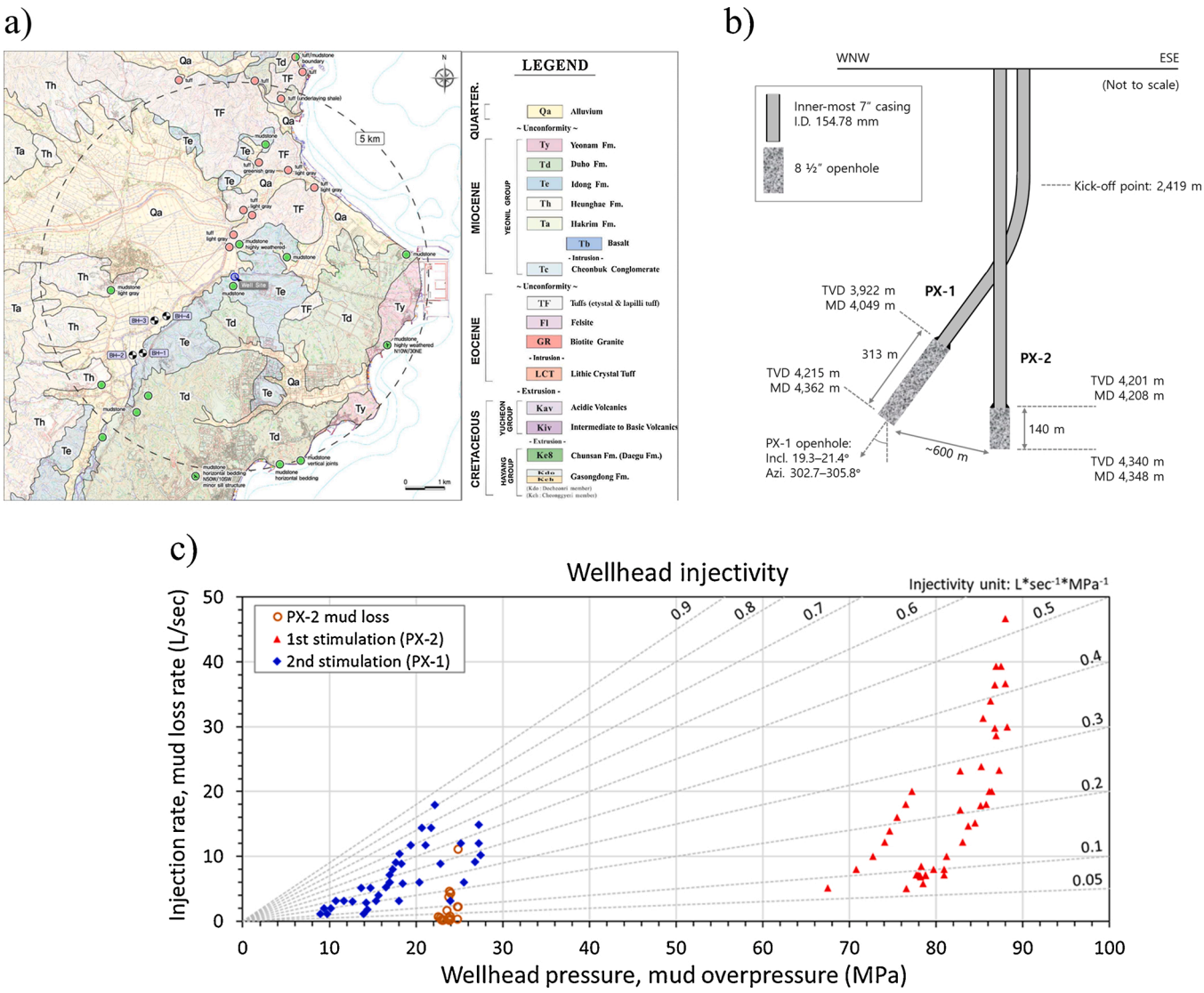

Fig. 1. (a) Geological map of the Pohang region including the location of the EGS site; (b) Schematic diagram of the two boreholes, PX-1 and PX-2, in the Pohang EGS site; (c) Comparison of the wellhead injectivity between the first and the second stimulations (Park et al., 2020).

dilation characteristics can be estimated through the calibration process. Numerical modeling has been extensively applied for analyzing hydraulic stimulations of various EGS project sites using a variety of numerical simulators, e.g., Desert Peak in Nevada, USA (Dempsey et al., 2015), the Geysers in California, USA (Jeanne et al., 2014), Soultz-sous-Forêts in France (Kohl and Mégel, 2007; Baisch et al., 2010), Newberry in Oregon, USA (Rinaldi et al., 2015; Cheng et al., 2019), the Fenton Hill in New Mexico, USA (Norbeck et al., 2018; Rinaldi and Rutqvist, 2019), and Groß Schönebeck in Germany (Blöcher et al., 2018).

During hydraulic stimulations in fractured porous EGS reservoirs, hydraulic properties such as fracture permeability and porosity change corresponding to stress and pressure changes as a result of fluid injection into the reservoir. Numerical simulators have been developed to simulate such interactions between hydraulic and mechanical processes in order to predict the hydro-mechanical and seismic responses. For example, continuum based analyses of such processes in fractured porous media have been conducted using finite element simulators, e.g., FRACure (Kohl and Hopkirk, 1995), OpenGeoSys (Kolditz et al., 2012) and GOLEM (Cacace and Jacquey, 2017), and finite volume simulators, e.g., FLAC3D (Itasca, 2009) and TOUGH-FLAC (Rutqvist, 2017). Discrete fractures also have been explicitly modeled for the analyses of the processes in fractured geothermal reservoirs such as shear slip and fracture propagation in discrete fracture network models using CFRAC (McClure and Horne, 2013, 2014), tensile and shear mixed-mode propagation using displacement discontinuity models (e.g., Kamali and Ghassemi (2018)), and fault reactivation by shear dilation and normal opening using the 3D distinct element code, 3DEC (Yin et al., 2020). However, hydraulic stimulation mechanism in fractured reservoirs is complex overprinted by various hydro-mechanical processes and there are still few numerical studies that mimic realistic hydraulic pressure responses from full-scale hydraulic stimulations.

A total of five hydraulic stimulations were carried out in the Pohang EGS project in South Korea (Park et al., 2020). On November 15, 2017, two months after the fifth hydraulic stimulation, the M_w 5.5 earthquake occurred at the Pohang EGS site. After a year of investigation, a government-appointed commission concluded that the M_w 5.5 earthquake was triggered by the hydraulic stimulations (Lee, 2019), making the Pohang earthquake the largest of its kind in EGS development. Currently, extensive studies are underway regarding the causal relationship between the earthquake and the EGS stimulation. Studies focusing on seismic analysis showed a close spatial-temporal relationship between induced seismicity by the hydraulic stimulation and the Pohang M_w 5.5 earthquake (Ellsworth et al., 2019; Woo et al., 2019).

Changes in poroelastic stress and pore pressure on the M_w 5.5 earthquake fault caused by the stimulation were studied by hydraulic or poroelastic continuum based numerical models (Chang et al., 2020; Lim et al., 2020; Yeo et al., 2020). These previous numerical studies were based on constant permeability models in a porous medium and did not include fracture fluid flow or permeability changes due to the hydraulic stimulations. Given prevalent fractures in the granodiorite host rock (Diaz et al., 2017; Kwon et al., 2019), fractures are believed to be the main pathways in the Pohang fractured reservoir. Moreover, the injectivity has been observed to be highly stress dependent during the hydraulic stimulations (Park et al., 2020). Therefore, consideration of fracture fluid flow and associated fracture permeability changes is critical in evaluating the mechanisms of hydraulic stimulations.

Park et al. (2020) presented key observations and analyses of the first and second stimulations conducted at the Pohang EGS site. The first two hydraulic stimulations are considered to be critical in understanding the Pohang fractured reservoir because these provide the first responses of the virgin reservoir that best depicts the reservoir characteristics. As a follow-up to Park et al. (2020), this study intends to improve the understanding on the mechanisms of hydraulic stimulations conducted in the Pohang geothermal reservoir through numerical analysis. Models were developed to include dominant fracture flows along fracture zones intersecting PX-2 and PX-1 having different orientations relative to the in-situ stress field. Comprehensive hydro-mechanical coupled numerical simulation was carried out for the early days of the first and second hydraulic stimulations. Special focus was given to the simulations of key wellhead pressure responses and the evaluation of the main stimulation mechanisms in the two wells.

2. The Pohang EGS site and the first and second hydraulic stimulations

The first EGS development project in South Korea was initiated in 2010 in Pohang, which is located in southeastern South Korea (Fig. 1a). The project aimed to generate approximately 1 MW of geothermal power in a doublet system by conducting hydraulic stimulation (Lee et al., 2011; Yoon et al., 2015). The reservoir consists of granodiorite below the depth of around 2.4 km, which is covered by a sequence of andesites and crystal tuffs, a 1 km thick Cretaceous sedimentary layer of sandstones and mudstones, and a 200 m–400 m thick Tertiary semi-consolidate mudstone (Lee et al., 2015). Two boreholes, PX-2 and PX-1, were drilled to the true vertical depth (TVD) of 4340 m and 4215 m, respectively (Fig. 1b). The PX-2 and PX-1 wells have a 140 m and 313 m open-hole section, respectively, and they are approximately 600 m apart at the bottomhole. Further details of the site and the hydraulic stimulations can be found in Park et al. (2020).

Among the five hydraulic stimulations carried out in the Pohang EGS site, the first hydraulic stimulation at the Pohang EGS site was conducted in the PX-2 well from January 29 to February 20, 2016, and the second stimulation was in the PX-1 well from December 15–28, 2016. The total volume of water injected into PX-2 was 1970 m^3 for the first stimulation and 895 m^3 of water was bled-off from the PX-2 well before the third stimulation. In the second stimulation, the injection volume to PX-1 was 3907 m^3 and 2164 m^3 of water was bled-off from PX-1 before the fourth stimulation. Various injection schemes and stimulation strategies have been implemented, including step rate tests, cyclic injections, continuous injections, long-term shut-ins, sudden high-rate injections, and bleed-offs (Park et al., 2020). A seismic monitoring system was installed to monitor and manage induced microseismic events during the hydraulic stimulations (Kim et al., 2018). The largest seismic events of M_L 1.7 and M_L 2.2 were observed in the first and second stimulations, respectively, according to the seismic data provided by the Korea Institute of Geoscience and Mineral Resources (KIGAM) (Park et al., 2020).

The hydraulic stimulations in the PX-2 and PX-1 boreholes produced distinctly different results in terms of wellhead pressure and injectivity as shown in Fig. 1c, suggesting different stimulation mechanisms (Park et al., 2020). In PX-2, the maximum wellhead pressure was 89.2 MPa with a relatively low injectivity. The low injectivity was thought to be due to wellbore damage caused by drilling, and the flow path through fractures connected with the borehole appeared to be blocked. The stimulation mechanism in PX-2 was interpreted to be normal fracture opening, involving a transition from fracturing or tensile extension to hydraulic jacking with a peak wellhead pressure at 64−67 MPa. In contrast, a higher injectivity was achieved in PX-1, and the maximum wellhead pressure was 27.7 MPa. Hydroshearing accompanying shear slip and dilation on the pre-existing fractures was highly likely to have occurred since clear pressure drops were observed at wellhead pressure as low as 15−17 MPa.

3. Methodology

3.1. Numerical simulator for coupled hydro-mechanical modeling

The TOUGH-FLAC simulator was used for coupled hydro-mechanical modeling of the Pohang geothermal reservoir. TOUGH-FLAC is a thermo-hydro-mechanical simulator (Rutqvist, 2017), which couples a simulator for multiphase fluid flow in a porous medium, i.e., TOUGH2 (Pruess et al., 2012) and a simulator for geomechanical processes, i.e., FLAC3D (Itasca, 2009). In this study, pore pressure was calculated in TOUGH2 and transferred to FLAC3D. FLAC3D updated the stress and strain in the model and determined plastic shear strain and dilation processes in a fracture zone. Hydraulic properties in the fracture zone were updated by applying the updated effective stress and plastic shear strain to a fracture permeability model and used for fluid flow calculation in TOUGH2. This process proceeded sequentially in all the steps of calculations (Rutqvist, 2017).

The TOUGH-FLAC simulator has been applied to hydro-mechanical modeling of stimulations in several geothermal development sites in the USA including Newberry Volcano in Oregon (Rinaldi et al., 2015), the Geysers in California (Jeanne et al., 2014), and Fenton Hill in New Mexico (Rinaldi and Rutqvist, 2019). The TOUGH-FLAC simulator has been widely applied considering stress-dependent permeability including fracturing and hydraulic shearing of fractures for geomechanics applications, such as investigation of seismicity, leakage and thermal effects associated with underground CO_2 sequestration (Rinaldi et al., 2014; Vilarrasa et al., 2017), hydraulic fracturing of shale-gas reservoirs (Rutqvist et al., 2015) and induced seismicity during natural gas production (Zbinden et al., 2017).

In this continuum-based TOUGH-FLAC code, several options exist for modeling thermo-hydro-mechanical processes in fractures and fractured rock. For example, in Rutqvist and Tsang (2003), intensively fractured volcanic tuff at Yucca Mountain, Nevada, was modeled in a dual-permeability continuum of matrix and fractures. Discrete fractures in a network would be explicitly considered by assigning different properties of continuum elements along the path of the fractures. Equivalent properties of these fracture elements are assigned to represent fracture permeability, stiffness, and strength, where shear and normal strains are related to fracture shear and normal displacements (Rutqvist et al., 2018). Besides, an anisotropic Mohr-Coulomb model can be used with weak planes along the local fracture plane orientation. This approach has been applied to simulate hydro-mechanical processes of faults in sedimentary host rocks (Cappa and Rutqvist, 2011; Rinaldi et al., 2015) and of a network of faults or fracture zones in crystalline rocks (Jeanne et al., 2014).

Due to the cubic-flow-aperture relation, the fracture flow is likely dominated by a fracture having the largest aperture even when multiple parallel fractures exist. Rinaldi and Rutqvist (2019) evaluated the effect of joint density in equivalent solid fracture element modeling by comparing two cases of fracture zones that embedded a single dominant fracture and ten fractures. In this study, we applied the solid element representation of fractures along a fracture zone. The geometry of the

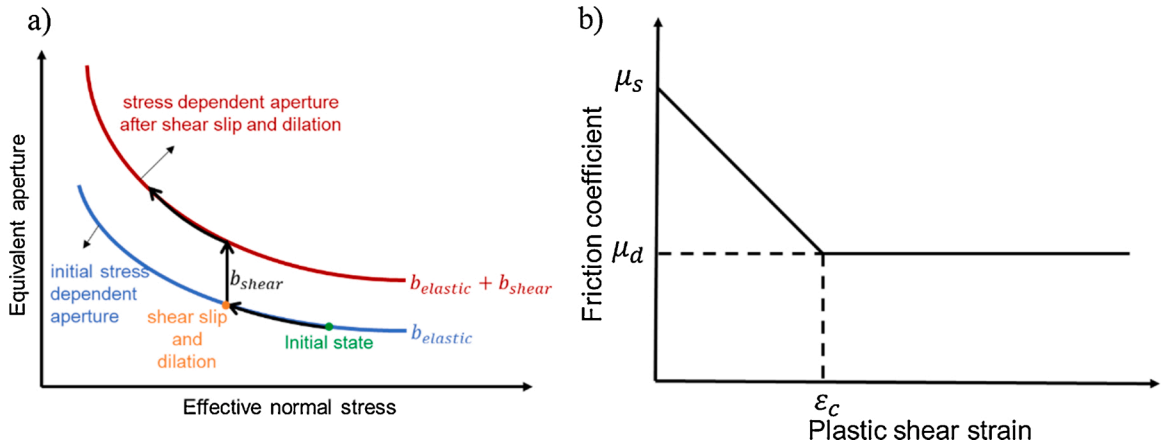

Fig. 2. (a) Conceptual diagram of equivalent aperture, describing its relation to effective normal stress and increase by shear dilation (redrawn based on Vilarrasa et al. (2017)); (b) the plastic shear strain-weakening friction law in the fracture zone (after Cappa and Rutqvist (2011)).

fracture zone was explicitly defined including the location and orientation, whereas the fracture opening and shear dilation of a dominant single fracture was implicitly modeled and evaluated from normal and shear strains of the fracture zone.

3.2. Fracture permeability model

In terms of elastic fracture responses, the equivalent hydraulic aperture of a single fracture or fractures within a fracture zone is related to an exponential function of effective normal stress according to the following equation (Rutqvist and Tsang, 2003):

$$b_{elastic} = b_r + b_{max}\exp(d\,\sigma_n^{'}) \quad (1)$$

where $b_{elastic}$ is the elastic hydraulic aperture, b_r is the residual hydraulic aperture, b_{max} is the maximum deformation of the aperture and d is a parameter related to the curvature of the aperture-stress curve. This equation enables to represent the jacking behavior of the fracture zone.

Shear slip and dilation in preexisting fractures within a fractured zone was modeled under the assumption that the flow occurred in one dominant fracture zone intersecting the openhole section of a well. Shear failure was governed by the Mohr-Coulomb failure criterion. Hsiung et al. (2005) derived an aperture change due to plastic deformation, such as shear dilation and tensile failure, in a continuum model of fractured rock. We assumed one dominant fracture, and shear dilation (b_{shear}) is calculated by

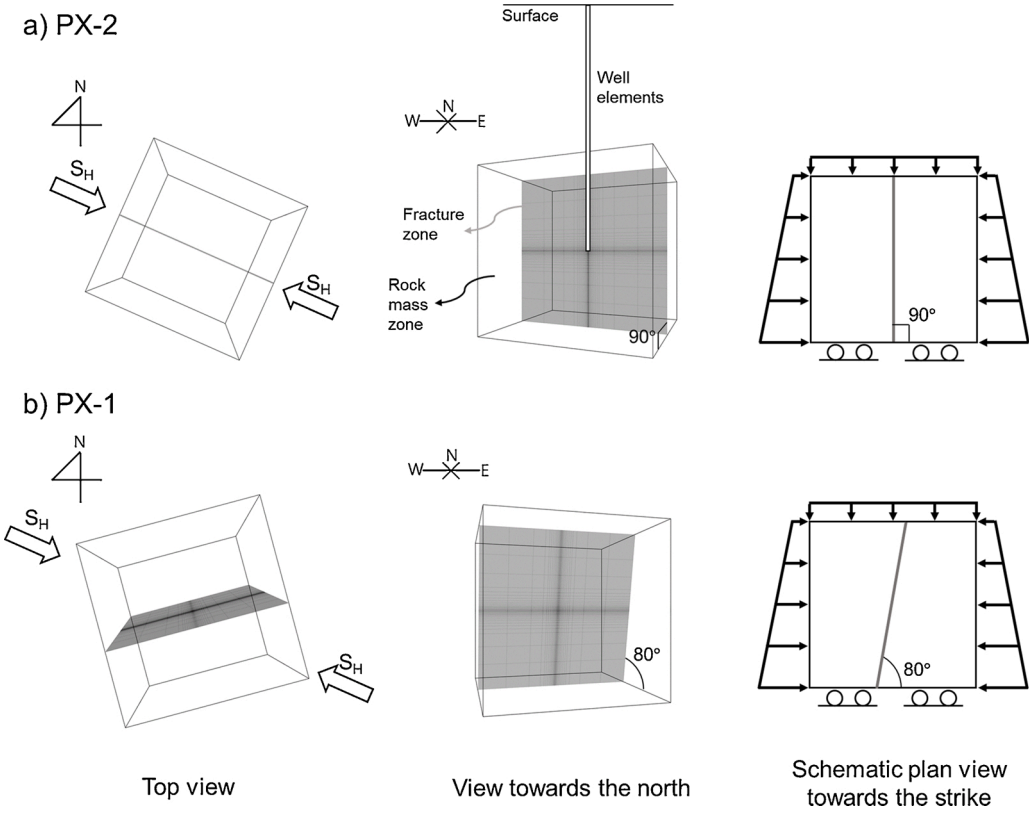

Fig. 3. Model configuration of (a) PX-2 and (b) PX-1; top view and view towards the north including the fracture zone and the surrounding rock mass; schematic plan view towards the strike showing the boundary and initial stress conditions.

Table 1
Propeties used both in the PX-2 and PX-1 simulations.

Properties		Value
Elastic modulus (GPa)*		33.49
Poisson's ratio*		0.21
Rock density (kg/m^3)*		2628
Porosity of rock mass*		0.0048
Permeability of rock mass (m^2)**		1×10^{-19}
Pore compressibility (GPa^{-1})**		3.6083
Biot coefficient**		1
In-situ stress model***	In-situ stress ratio ($S_{Hmax}/S_V/S_{hmin}$).	1.27/1.00/0.75
	Gradient of vertical stress (MPa/km)	25.7
	Gradient of maximum horizontal stress (MPa/km)	32.7
	Gradient of minimum horizontal stress (MPa/km)	19.2
	Azimuth of maximum horizontal stress (°)	114

* Kwon et al. (2019).
** Typical values were taken.
*** loosely based on Kim (2017).

$$b_{shear} = L\,\varepsilon_s\,tan\varphi \tag{2}$$

where L is the thickness of the solid fracture elements, which may represent the thickness of a fracture zone, ε_s is fracture plastic shear strain, and φ is the shear dilation angle of the fracture.

Hydraulic aperture was calculated as the sum of the shear dilation and elastic hydraulic aperture:

$$b = b_{shear} + b_{elastic} \tag{3}$$

Fig. 2a shows that the hydraulic aperture of a fracture follows the exponential function of the effective normal stress in the form of Eq. (1) and once the fracture shears, it starts to follow a new aperture function increased by the shear dilation as in Eq. (3).

The equivalent permeability of the continuum fracture elements that represents the permeability of one singe or several sub-parallel fractures within a fracture zone is obtained by applying the hydraulic aperture in the cubic flow law (Witherspoon et al., 1980):

$$k = b^3/12L \tag{4}$$

where L could either be equal to the size for the continuum element normal to the flow path or represent the spacing between several parallel and equally spaced fractures. In this study, we assume that the flow occurred along one dominant fracture along the fracture zone so that L would be equal to the size of the continuum fracture elements.

In order to describe a sudden shear slip, a strain-softening joint model was used in the fracture zone by linearly weakening the friction coefficient of an element after shear slip appears in the element (Itasca, 2009). The friction angle is maintained at a residual friction angle once the plastic shear strain reaches a critical shear strain, ε_c (Fig. 2b). The residual dynamic friction angle and the critical plastic shear strain are parameters that affect the onset and the extent of the area of the shear slip (Rutqvist et al., 2015). The maximum shear dilation is defined as

$$\max(b_{shear}) = L\,\varepsilon_c\,tan\varphi \tag{5}$$

This approach that combines shear dilation with frictional plastic strain softening and jacking behaviors in the TOUGH-FLAC simulator was previously used for the Fenton Hill injection experiment (Rinaldi and Rutqvist, 2019).

3.3. Description of PX-2 and PX-1 models

The three-dimensional models (Fig. 3) used in this study consist of a fracture zone, the surrounding rock mass, and well elements similar to a previous study (Rutqvist et al., 2015). The size of the model was 4 km × 4 km × 4 km, which was large enough not to disturb the boundary stress and pore pressure during the simulation. The fracture zone was positioned to intersect the center of the openhole section. The intersecting element of the openhole and fracture zone was located at the center of the model. The grid length of the fracture zone was 0.5 m–20 m for the PX-2 and 5 m–20 m for the PX-1 within a distance of 130 m from the borehole with finer grids near open holes. Well elements that connect the ground surface to the fracture zone were used only in TOUGH2, and water was injected into the top element of the well. For each of the two wells, the total volume of the well elements and fracture elements connected to the well was calibrated to match the wellhead pressure gradients with respect to time during the initial phase of injections. The calibrated volume was markedly different in the two models; 89 m^3 (85 m^3 of well elements and 4 m^3 of connected fracture elements) and 1121 m^3 (121 m^3 of well elements and 1000 m^3 of connected fracture elements) in the PX-2 and PX-1 models, respectively. This suggests contrasting hydraulic connections to surrounding rock in the two boreholes. Such a difference is consistent with an analysis of wellhead responses with respect to the increment of injected volume by Park et al. (2020).

Table 2
Fracture zone properties used in the PX-2 and PX-1 simulations.

Properties		Values	
		PX-2	PX-1
Porosity		0.0048	
Fracture zone thickness (m)		1	10
Dip / dip direction		90/024	80/345
Mechanical model		Elastic model	Bilinear strain-softening joint plastic model
Elastic hydraulic aperture of fracture zone ($b_{elastic}$)	b_r (μm)	7.0	3.0
	b_{max} (m)	2.25×10^{-5}	0.2435
	d (MPa^{-1})	6.15×10^{-2}	1.75×10^{-1}
Initial joint friction angle (°)*		–	26.6
Residual joint friction angle (°)		–	25
Dilation angle (°)		–	1
Critical plastic shear strain		–	0.0002
Maximum shear dilation (μm)**		–	35

* Kwon et al. (2019).
** Equation (5).

Properties applied both in the PX-2 and PX-1 models are listed in Table 1. Hydrostatic pore pressure was applied for the initial condition, and constant pore pressure was applied on the boundaries. The ground temperature and the temperature gradient were assumed to be 20 °C and 32 °C/km, respectively. In this study, the temperature of the rock was assumed to be constant, and thermal stress was not considered. However, the temperature was still taken into account to determine the water properties in TOUGH2. A fixed stress boundary condition was applied on the top and lateral boundaries, while a roller boundary was applied on the bottom. The surrounding rock mass was assumed to have constant mechanical and hydraulic properties, which were obtained from laboratory tests of rock cores from PX-2 (Kwon et al., 2019). Permeability for the rock mass was assumed to be 1×10^{-19} m^2 as a typical value for intact granodiorite. Therefore, pore pressure diffusion to the rock mass was almost negligible.

Several in-situ stress models have been suggested for the Pohang EGS site based on hydraulic fracturing stress measurements, focal mechanisms of induced seismicity, acoustic emission (AE) tests, core disking analyses on the recovered core samples and the Pohang M_w 5.5 earthquake (Park et al., 2020). The in-situ stress condition in this modeling was loosely based on the study by Kim (2017) with the maximum horizontal stress azimuth of 114° and the in-situ stress ratio of 1.27/1.00/0.75 ($S_{Hmax}/S_V/S_{hmin}$). As direct borehole observations through image logs were not carried out, and constraining data from borehole breakout or intersecting fracture orientations were not

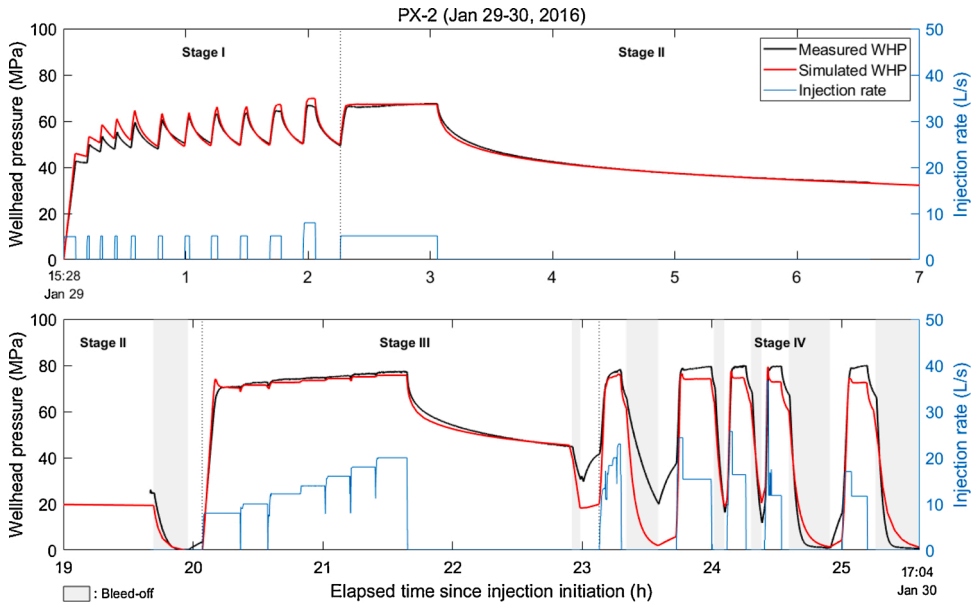

Fig. 4. Simulated and measured wellhead pressure of the first 25.6 h of the hydraulic stimulation in PX-2. Shadowed with light grey are bleed-off periods.

obtained. Therefore, it is emphasized that neither the in-situ stress condition nor the orientation of intersecting fractures or fracture zones adopted in the current modeling was meant to be conclusive. Rather, the combined choice of in situ stress and the orientation of intersecting fracture was intended to reproduce the observation of pressure responses during the hydraulic stimulations in the two boreholes.

For modeling of hydraulic stimulations in the two boreholes, two different geometrical models were established separately with different fracture orientations (Fig. 3 and Table 2). For the PX-2 stimulation, the fracture zone was assumed to be vertical and perpendicular to the minimum horizontal stress. (Fig. 3a). The choice of a vertical fracture zone was based on the observation of highly dipping fractures found at the rock core retrieved from the PX-2 well at the depth of 4219.0–4222.6 m, which belongs to the openhole section (Kwon et al., 2019). Both of the rock mass and fracture zone were modeled to behave elastically. The hydraulic aperture parameters in the PX-2 model, listed in Table 2, were obtained from calibration through a history matching of wellhead pressure.

In the geometrical model of the PX-1 stimulation, dip and dip direction of the fracture zone was assumed to be 80° and 345°, respectively (Fig. 3b), which was chosen to match the wellhead pressure drop around 16 MPa at the given in-situ stress state. Although it was reported that there was a likelihood that fracture zones existed with a dip of 65~70° and dip direction of 20~30° (Lee et al., 2007; Park et al., 2017), this was not validated with the spatial distribution of microseismicity during the injection. In the absence of direct observation in the borehole, there are uncertainties in the direction of intersecting fractures and the fracture zone. Therefore, the orientation chosen for the geometrical model of the PX-1 stimulation was valid only in the sense that it is vulnerable for shear slip with the corresponding injection. The initial joint friction angle of 26.6° was obtained from laboratory tests (Kwon et al., 2019). The other properties for the fracture zone were obtained from calibrations through a history matching of wellhead pressure following a similar procedure used for PX-2 modeling.

4. Simulation results and discussion

4.1. The first hydraulic stimulation at the PX-2 well

4.1.1. History matching in the borehole

Coupled hydro-mechanical modeling was carried out on the first 26 h of stimulation at the PX-2 well, which was composed of four stages in two days. On the first day, injections at a rate of 4−8 L/s followed by shut-ins underwent eleven cycles with durations of less than 10 min per cycle (Stage I), followed by the final cycle of 48 min of injection and a shut-in (Stage II). Step rate injection (Stage III) and sudden high rate injection and bleed-offs (Stage IV) were implemented on the second day.

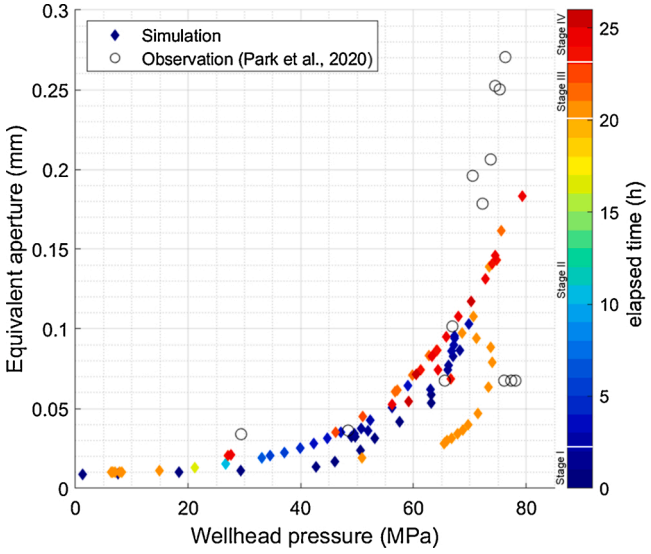

Fig. 5. Simulated and observed equivalent apertures against wellhead pressure in the PX-2 stimulation. Colored dots indicate equivalent apertures at the bottomhole obtained in the numerical modeling. Empty dots are equivalent apertures of the reservoir calculated from measured wellhead pressure (modified from Park et al. (2020)).

The measured and modeled wellhead pressures were in a good match as shown in Fig. 4. A slight wellhead pressure drop was observed at around 67 MPa at the last two cycles of injections during Stage I in the field, and this moderate breakdown indicates a possible hydraulic fracturing or opening of pre-existing fractures (Park et al., 2020). Numerical modeling showed stabilized pressure rather than pressure drop because the permeability increase was smooth in numerical modeling due to the use of exponential stress dependent permeability.

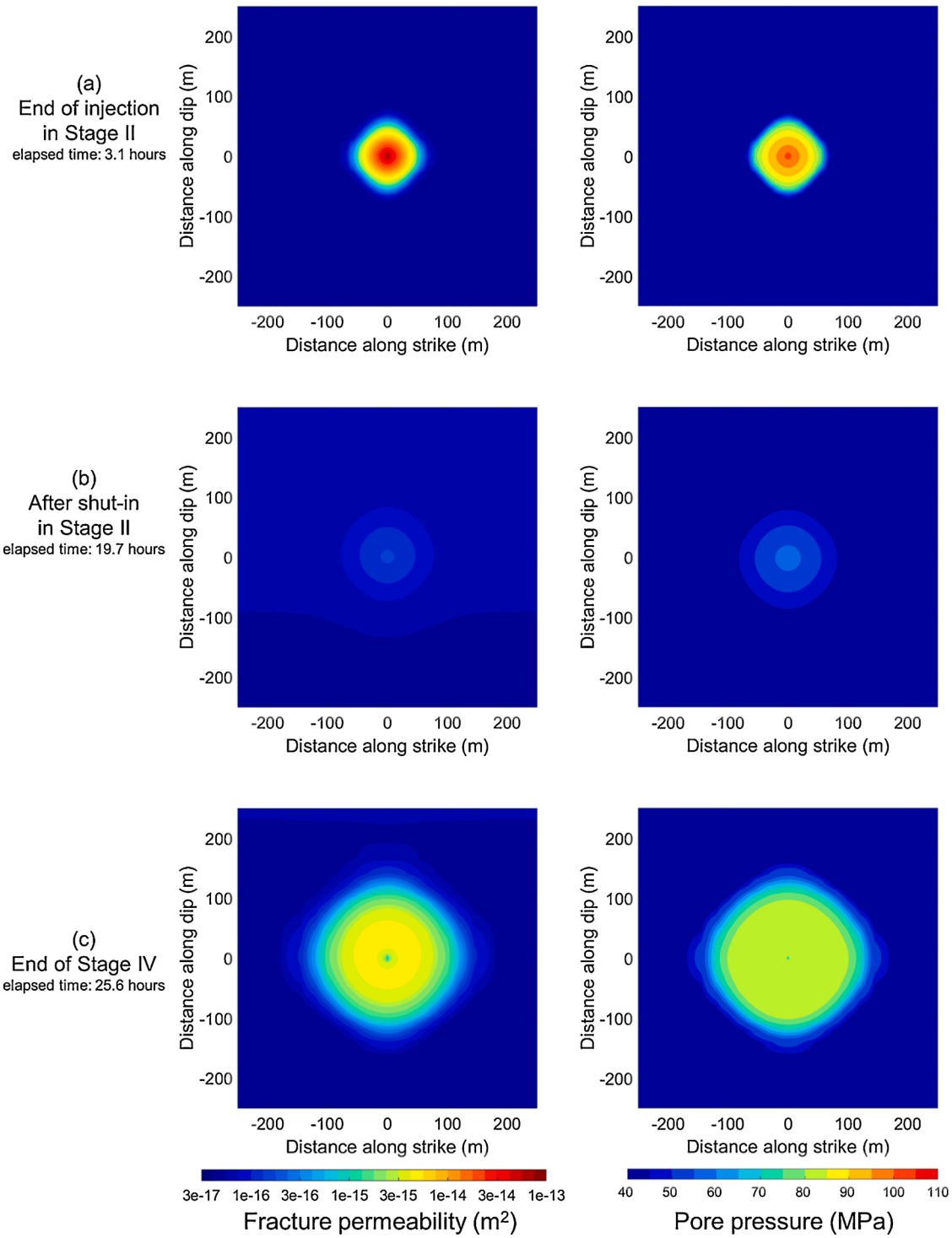

Fig. 6. Magnified contour diagrams of permeability and pore pressure on the fracture zone in the PX-2 model. The center of each diagram is the intersection between the well and fracture zone.

Nevertheless, numerical modeling captured the distinct pressure response at 67 MPa.

In Stage III, the simulated pressure curve generally matched the measured wellhead pressure during the step-rate increases of flow rate and shut-in. There were frequent bleed-offs in Stage IV as shown by drastic decreases of pressure. The bleed-off was numerically modeled to a reasonable extent by calibrating the productivity index of the deliverability model in TOUGH2 (Pruess et al., 2012). Because the exact amount of each bleed-off was not precisely measured at the site, an identical productivity index was assumed for all of the bleed-offs, resulting in some discrepancies. As the stimulation continues, small discrepancies between measured and modeled pressure were consistently observed in the order of around 5−8 MPa for the last four cycles of injections in Stage IV. The simulated pressure for those periods stabilized in the range of 72–75 MPa, whereas the measured pressure went up to 80 MPa. As the current numerical model is composed of one single fracture zone intersecting the borehole, the discrepancy between the measured and simulated pressure responses may be attributed to the

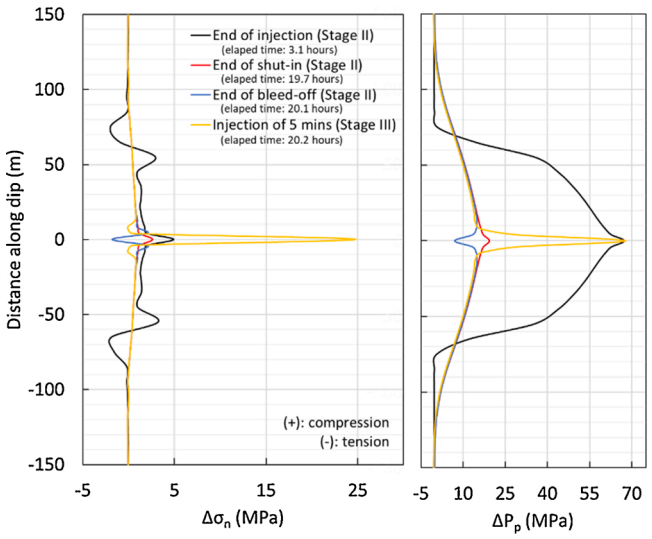

Fig. 7. Changes in simulated normal stress and pore pressure in the fracture elements along the dip of the PX-2 model, intersecting the injection element at 0 m.

limited knowledge in the fracture geometry and permeability away from the borehole.

In Fig. 5, the simulated equivalent aperture was compared with the ones obtained from the field observations (Park et al., 2020). The simulated apertures were taken from the evolution of the fracture elements intersecting the borehole, whereas the ones from the field observations represented the transmissivity of a reservoir system affected by injection. Highly reversible non-linear aperture change noted from the field interpretation of the hydraulic stimulation was successfully realized in the numerical modeling as the hydraulic aperture was governed by an exponential function of effective stress, Eq. (1). The maximum equivalent aperture at the bottom hole in the PX-2 modeling reached 0.18 mm, about 20 times as large as the minimum aperture. Since total stress on the fracture zone continuously changed due to poroelastic effects as presented later, the simulated equivalent apertures at similar pressure levels were scattered slightly as was also observed from the field interpretation.

4.1.2. *Responses in the stimulated fracture zone*

Pore pressure and permeability distributions within the fracture zone are shown in Fig. 6. Overall, the changes in permeability correlated well with pore pressure changes because of the stress-dependent permeability model implemented in the current study. At the end of the injection in Stage I when about 26 m^3 of water had been injected, the calculated permeability increased by about three orders of magnitude, from 10^{-16} m^2 to 10^{-13} m^2 at the injection point. The calculated permeability was about 10^{-14} m^2 and 10^{-15} m^2 at 31 m and 53 m from the injection well, with the corresponding pressure increase of about 52 MPa and 41 MPa, respectively (Fig. 6a). During the shut-in from 3.1–19.7 h in Stage II, pressure diffusion still continued, and an overpressure front of 0.5 MPa reached 132 m from the injection well. While permeability recovered close to the initial level, the maximum overpressure of 19 MPa still remained in the fracture zone (Fig. 6b). At the end of Stage IV, the disturbed pressure area expanded farther with an overpressure front of 0.5 MPa at a horizontal distance of 180 m. As pressure diffused more, permeability was in the order of 10^{-15} m^2 within 109 m from the injection well. Because injected water had been flowed back, pressure and accordingly, permeability near the well became smaller, whereas it was higher in the surrounding area (Fig. 6c).

Simulated normal stress in the fracture zone was disturbed by the poroelastic effect during the PX-2 stimulation. Fig. 7 shows changes in fracture normal stress and pore pressure in the fracture zone at various stages. The area with an increase and decrease in normal stress corresponded to an increase and decrease in pore pressure, respectively.

At all the observations, the amount of normal stress change was larger when the pore pressure gradient was greater. The ratio of poroelastic stress change to pressure change is defined as the stress path coefficients in reservoir geomechanics (Fjær et al., 2008; Zoback, 2010). According to Segall and Fitzgerald (1998), the stress path coefficient is related to the shape of the reservoir, which corresponds to a pressurized volume in the fracture zone in the current study. The aspect ratio of the pressurized volume is small at the initial stage of injection but it becomes larger as the injection continues. The stress path coefficient to the shorter-side direction of the reservoir, which is the fracture normal direction in this study, decreases as the aspect ratio of the reservoir increases. At five minutes after the start of the injection in Stage III, the injection resulted in a significant local increase in pore pressure as large as 67 MPa. The local pressure increase induced a normal stress increase of 25 MPa with a stress path coefficient of 0.37. In contrast, at the end of injection in Stage II, the normal stress increased by 5 MPa even though the overpressure was the same as after the five-minute injection in Stage III. The stress path coefficient at this moment was as low as 0.07 because the aspect ratio of the pressurized volume increased after the relatively longer injection in Stage II. The large increase in normal stress at the injection initiation of Stage III caused smaller equivalent aperture at the wellhead pressure range of 65–75 MPa when compared to other stages, as depicted in orange color dots in Fig. 5.

As the complete characterization of the fractured reservoir was challenging, uncertainties associated with the current numerical modeling merits further discussion. The uncertainty in the current modeling includes i) the orientation of the intersecting fracture, ii) the representative thickness of the fracture zone, and iii) reduced fracture permeability due to hydraulic damage of the reservoir.

The magnitude of fracture permeability was estimated by pressure history matching with the point-wise injection in the vertical fracture based on the high-dipping fractures observed in the rock cores (Kwon et al., 2019). While this assumed that the injection may occur on a small area of the intersection of the borehole and the vertical fracture, the actual injection may occur at the longer longitudinal section of vertical fractures. In such a case, the spatial evolution of pore pressure and permeability would be different from the point-wise injection (Yoo, 2018). Furthermore, there is a possibility of the creation of new tensile fractures through hydraulic fracturing either in a vertical or horizontal direction.

It is thus difficult to estimate the thickness of the fracture zone utilized for the flow path among the 140-m openhole. If the fracture zone was thicker, the pressure would have diffused in narrower areas due to a reduction of calibrated permeability, and, vice versa. Changes in the fracture zone thickness would vary calibrated equivalent aperture due to the cubic law and storativity changes. Therefore, an alternative model with different fracture zone thickness would lead to a different set of apertures and storativity.

Hydraulic damage of the reservoir by heavy mud weight and lost circulation material (LCM) during the drilling was noted as the main cause responsible for the lower injectivity in PX-2 when compared to PX-1 (Park et al., 2020). The LCM material may have been pushed further during the continued injections, thus reducing the fracture permeability farther from the wellbore. Current modeling did not attempt to consider the mass transport of LCM into the reservoir. Yoo (2018) conducted numerical modeling of the PX-2 stimulation including the reservoir damage near the well, but history matching of the pressure curve alone could not determine a unique combination of damage magnitude and area.

4.2. *The second hydraulic stimulation at the PX-1 well*

4.2.1. *History matching in the borehole*

Coupled hydro-mechanical modeling was carried out on the first 46 h

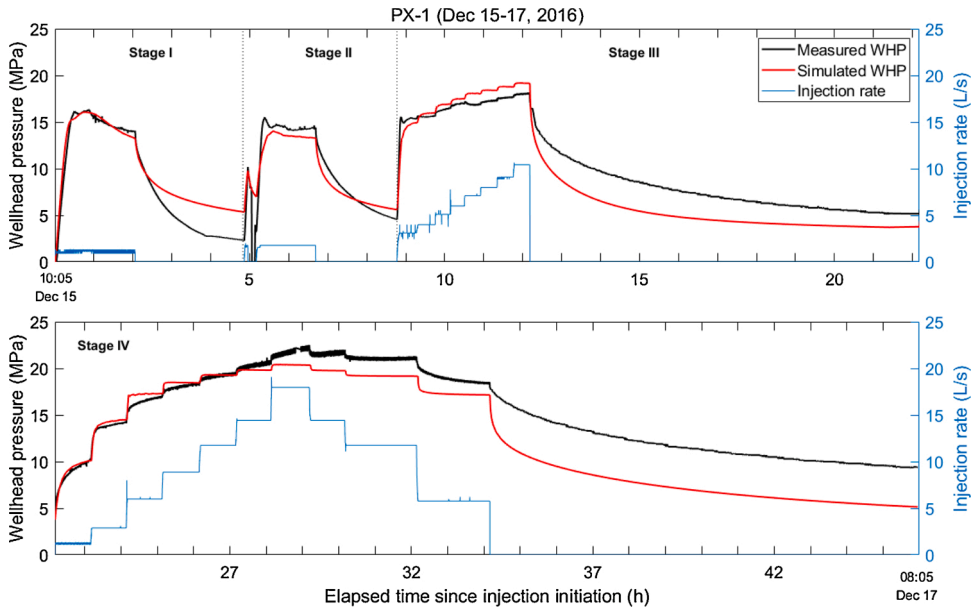

Fig. 8. Simulated and measured wellhead pressure of the first 46 h of the hydraulic stimulation in PX-1.

of stimulation at the PX-1 well, which is composed of four stages in nearly two full days. On the first day, a clear breakdown pressure was observed at 16 MPa when the injection rate was around 1 L/s in Stage I, which was explained by the hydraulic shearing of the pre-existing fracture. During Stage II, a similar fracture shear slip behavior was observed with an injection of 1.8 L/s with a smaller pressure drop. In Stage III, with a step rate increase from 3.1 L/s to 10.4 L/s, a gradual increase of pressure from 15 to 18 MPa was observed with increasing injection rates. On the second day, the injection rate was step-wisely increased from 1.1–14.4 L/s and then decreased to 5.8 L/s (Stage IV) (Park et al., 2020).

Fracture shear dilation and frictional plastic strain softening model adopted in the current study achieved a remarkable similarity with the observed pressure evolution on the first day as shown in Fig. 8. The breakdown pressure at 16 MPa and clear pressure drop during Stage I were reproduced with a very good match. The continued propagation of the fracture shear slip area successfully captured the observed pressure evolution with a less pressure drop at Stage II than at Stage I. The gradual pressure increase during Stage III was well simulated by the combination of the continuous increase of the sheared area and hydraulic jacking following the stress dependent permeability. The simulated pressure reduced more than the measured pressure especially during the shut-in in Stage III hinting a possible presence of low permeable zone away from the injection well. This motivated us to carry out an additional sensitivity study as presented later.

The general trend of the pressure curve was captured in the simulation of Stage IV. The pressure responses were mainly governed by the hydraulic jacking of the shear-dilated fracture as well as the progress of shear dilation into new fracture areas. The discrepancies occurred mainly during the step-down period of the injection. The observed wellhead pressure responses were not the same during the step-up and step-down periods even at the same injection rates. Converging pressures during step-down periods were greater than the ones during step-up periods by a few MPa. However, in the simulation, converging wellhead pressure during increasing and decreasing step rates were similar when compared at a similar level of flow rates, which demonstrates the discrepancy between observation and modeling. In addition, the measured pressure was consistently larger than the simulated pressure during the shut-in of Stage IV. Those differences indicate that the fracture zone in the reservoir may have non-uniform hydro-mechanical characteristics and can be more complex than a homogeneous single fracture zone.

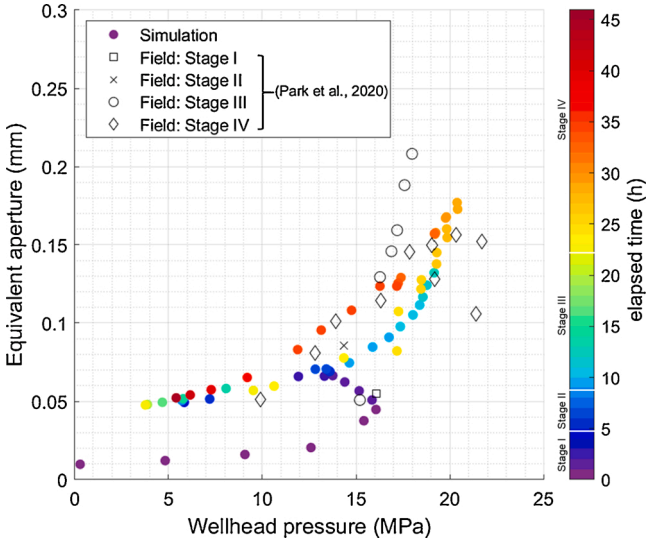

Fig. 9. Simulated and observed equivalent apertures against wellhead pressure in the PX-1 stimulation. Colored dots indicate equivalent apertures at the bottomhole obtained in the numerical modeling. Empty dots are equivalent apertures of the reservoir calculated from measured wellhead pressure (modified from Park et al. (2020)).

The behavior of simulated equivalent apertures at the injection fracture element was presented in Fig. 9 with respect to wellhead pressure in PX-1 together with the field data from Park et al. (2020). The simulated equivalent apertures were comparable with the ones from the field analysis. Starting the injection in Stage I, the simulated equivalent aperture gradually increased following an exponential function of effective normal stress. Reaching around 12−16 MPa of wellhead pressure in Stage I, the simulated equivalent aperture was enhanced about 3.6 folds through a combination of shear dilation and fracture opening from approximately 0.018 mm to 0.065 mm.

In Stages II-IV, the equivalent aperture at the injection fracture element appeared to be following a shifted exponential curve similar to the one shown in Fig. 2a. Reversible non-linear aperture changes of the shear-dilated fracture were simulated in those stages. The simulated

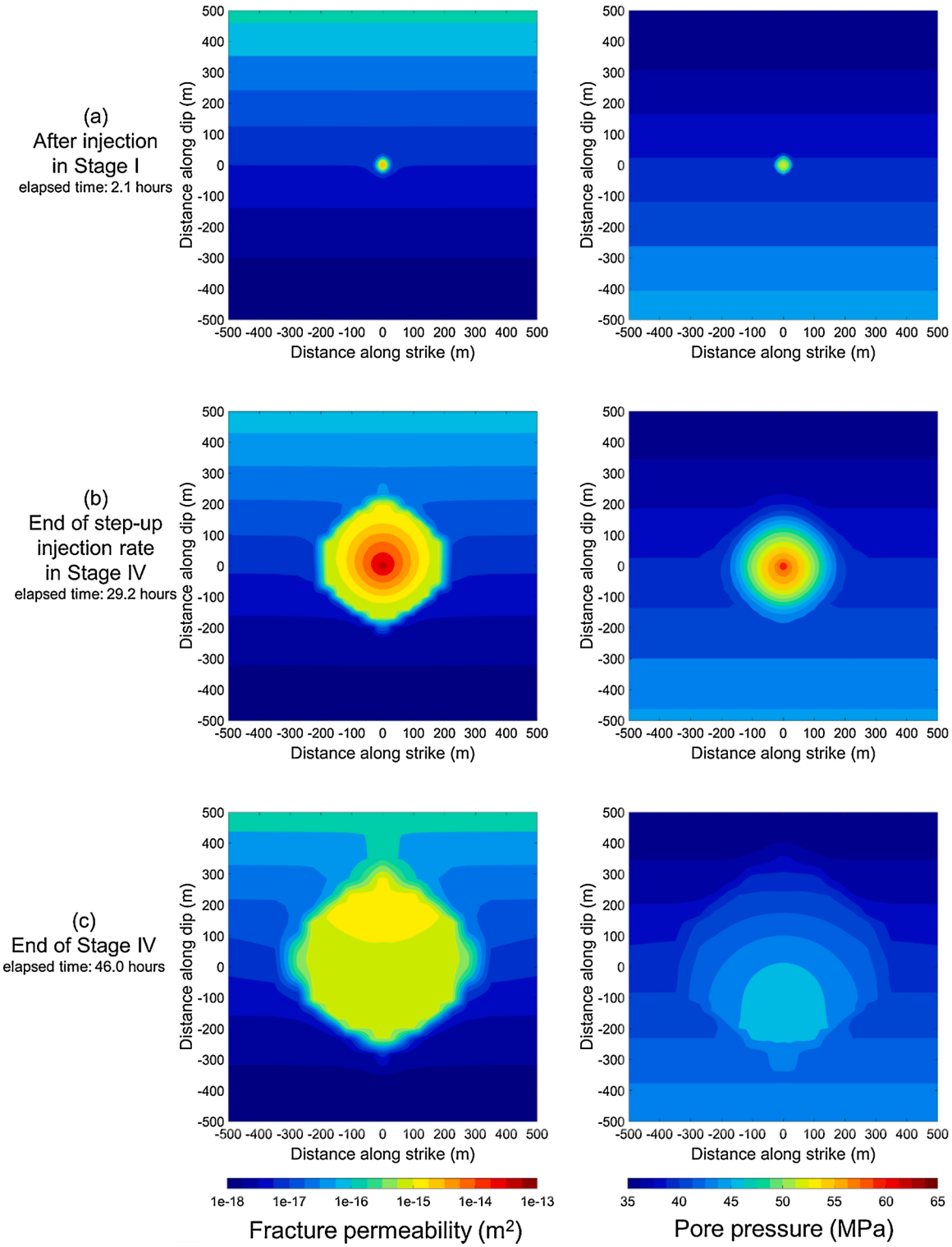

Fig. 10. Magnified contour diagrams of permeability and pore pressure on the fracture zone in the reference PX-1 model. The center of each diagram is the intersection between the well and fracture zone.

equivalent aperture increased up to 0.18 mm at 20.4 MPa in Stage IV and returned to 0.05 mm, which is considered to be a residual aperture after shear dilation. The continuous change in total stress caused variable apertures at the same wellhead pressure because of the poroelastic effect, as was also observed in Fig. 5.

4.2.2. Responses in the stimulated fracture zone

Pressure evolutions and changes in permeability in the fracture zone are shown in Fig. 10. In the fracture zone of PX-1, permeability was governed by shear dilation as well as effective normal stress. When the injection stopped during Stage I, the overpressure front of 0.5 MPa advanced 35 m from the injection well in the horizontal direction. (Fig. 10a). At the end of the step-rate increase at 29.2 h in Stage IV, the overpressure had a maximum value of 20 MPa. The overpressure front of 10 MPa and 0.5 MPa reached 110 m and 224 m, respectively, from the injection point. Shear dilation enhanced the permeability to more than

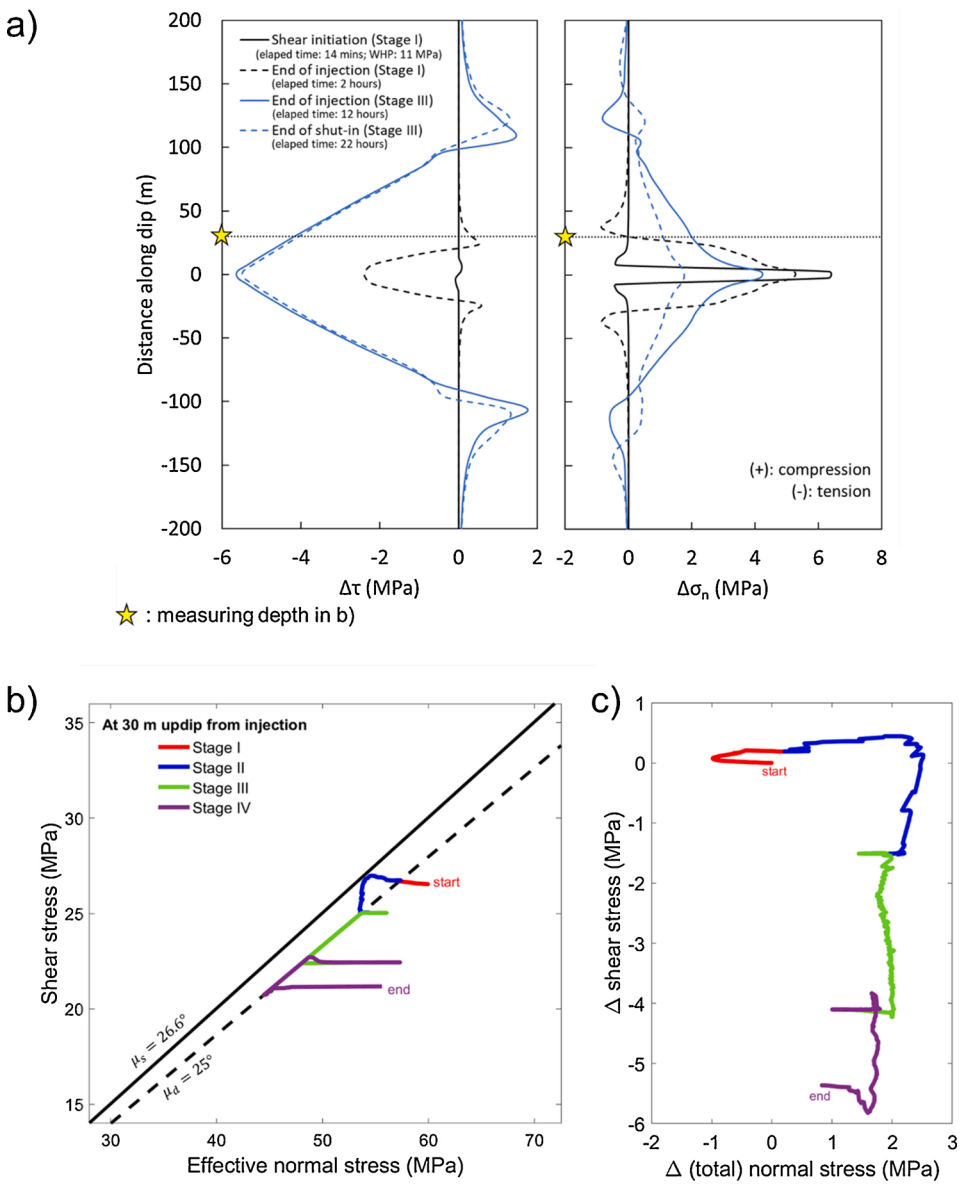

Fig. 11. (a) Changes in shear and normal stress in the fracture elements along the dip of the PX-1 reference model (C1) when the injection element intersected at 0 m; (b) Stress path of shear and effective normal stress with failure criteria with initial and residual joint friction angles; (c) Changes in shear and normal stress from the initial state. (b) and (c) were monitored at 30 m upward along the dip from the injection point as a representative point, marked with a yellow star in (a) (For interpretation of the references to colour in this figure legend, the reader is referred to the web version of this article).

10^{-15} m^2 within a radius of about 180 m. Permeability increased to the order of 10^{-14} m^2 close to the injection point by additional jacking (Fig. 10b). Pressure diffusion continued during the shut-in period in Stage IV and extended an overpressure front of 0.5 MPa to a radius of 349 m. Furthermore, the magnitude of permeability was maintained as large as 10^{-15} m^2 to 225 m from the injection point because of permanent permeability enhancement by shear dilation (Fig. 10c).

The PX-1 fracture zone experienced changes in both shear stress by plastic shear slips and normal stress by poroelastic effects. Fig. 11a shows changes in shear and normal stress in the fracture zone at various times of injection. While the process of normal stress changes was similar to the PX-2 model, changes in shear stress were different. When it was about to start a shear slip right after injection started, there were no changes in shear stress and only local normal stress was increased by up to 6 MPa due to poroelastic effects near the well. Once shear slip occurred, shear stress dropped by more than 2 MPa near the injection well. A smaller increase of shear stress was also noted at the edge of the shear stress drop area at the end of injection in Stage I. As the hydraulic stimulation continued, shear stress decreased by nearly 6 MPa and its areal range of change was greater. At the end of the shut-in in Stage III, the shear stress change was irreversible whereas the normal stress recovered as the pore pressure recovered in comparison to the state of the end of injection in Stage III.

Fig. 11b shows the stress path at a selected point in the fracture zone which is 30 m away from the injection point along the dip of the fracture zone. The changes in total normal stress and shear stress at the selected point during Stage I-IV are presented in Fig. 11c. This point further away from the injection well was chosen for the numerical investigation into the injection-induced hydro-mechanical behavior of the fracture zone that was not monitored during the observation from the surface. While shear slip occurred during Stage I near the injection well, it was during Stage II when the shear slip occurred at this selected point since it was 30 m away from the injection well.

Interestingly, as injection continued in Stage I, the normal stress first dropped and then started to increase. As injection continued in Stage II, shear stress increased because of the approach of the shear slip front. The increase in normal stress led to an increment of required pore pressure for a shear slip initiation at the point. At the same time, the increase in shear stress facilitated the shear slip initiation. The stress state satisfied the failure criterion with an initial joint friction angle of 26.6° and shear stress dropped through the slip weakening by about 2 MPa. Thus in Stages III-IV, the failure criterion with a residual joint

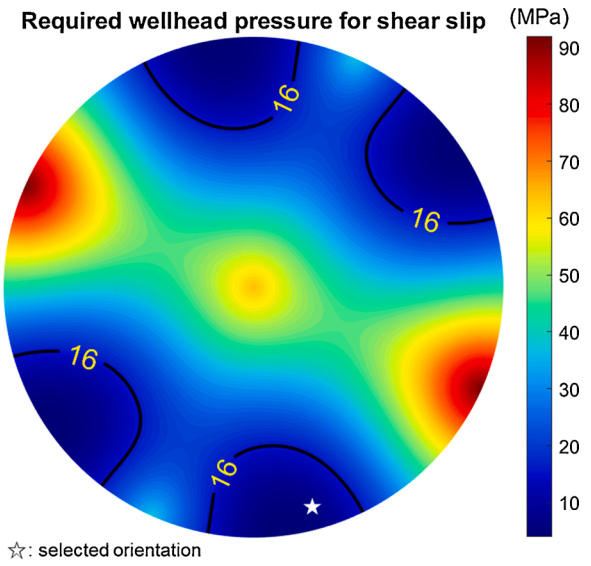

Fig. 12. Required wellhead pressure for shear slip at the bottom hole of PX-1 under the initial in-situ stress condition. The distribution was drawn on a stereonet applying the equal-area projection to the lower hemisphere. The black line indicates the fracture orientations which require wellhead pressure of 16 MPa for shear slip. The white star is the selected fracture zone orientation in this study and its required wellhead pressure was 6 MPa (dip/dip direction of 80/345).

friction angle of 25° governed the shear slips and the total amount of shear stress drop was about 6 MPa. Moreover, the stress state temporally became stable with increases in normal stress, and the stress state went away from the failure criterion during the shut-ins. This numerical investigation in the selected point shows that the local stress in the PX-1 model was continuously changed by the combination of the poroelastic effect and frictional-weakening shear slips.

4.2.3. *Critical pressure for shear slip considering the poroelastic effect*

Critical wellhead pressure for shear slip was calculated under the initial in-situ stress state at different fracture orientations as shown on a stereonet in Fig. 12. If the initial stress state had maintained constant without the poroelastic effect, the critical wellhead pressure for shear slip would have been around 6 MPa as indicated by a white star at the fracture orientation of 80°/345°. However, the coupled numerical analysis showed that the onset of shear slip was observed at a wellhead pressure of 11 MPa which is 5 MPa larger than the prediction by shear slip potential analysis. This was explained by the increased total normal stress by 5 MPa driven by poroelastic effect in as shown in Fig. 13. Even after the onset of shear slip at 11 MPa, the wellhead pressure continued to increase until the shear slip area and dilation became large enough to lead to a pressure drop at 16 MPa in Stage I. Both of the pressure at the onset of shear slip and the peak pressure were larger than the critical wellhead pressure predicted by the analytic calculation based on the initial stress state. This shows that coupled hydromechanical analysis is necessary for accurate estimation of critical pressure for shear slip and simple shear slip potential analyses may underestimate the critical wellhead pressure.

The change of total stress corresponding to pore pressure change has been of considerable interest in reservoir geomechanics (Segall and

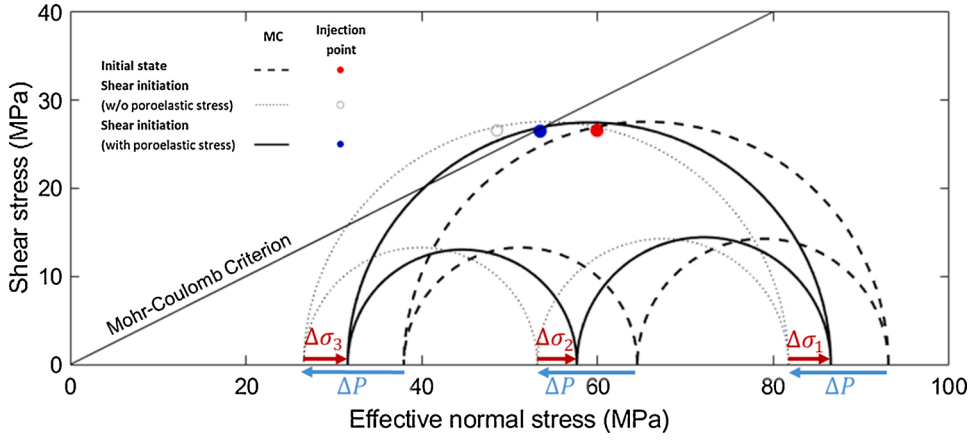

Fig. 13. 3D-Mohr circles representing stress state at a grid point of a fracture zone element intersecting the PX-1 well; dashed line at the initial state, and solid and dotted lines at the onset of shear slip (11 MPa of WHP). While the solid line included the poroelastic effect considering changes both in total stress and pore pressure, the dotted line did not.

Table 3
Fracture zone properties for different PX-1 modeling scenarios.

		C1 (Reference)	D1	D2	D3	C2	
Hydro-mechanical model		shear slip and dilation + elastic jacking	shear slip and dilation			shear slip and dilation + elastic jacking	
Spatial uniformity of permeability model		uniform				non-uniform	
						r < 75 m	r > 75 m
Elastic hydraulic aperture of fracture zone ($b_{elastic}$)	b_r (μm)	3.0	20.0			3.0	1.5
	b_{max} (m)	0.2435	0			0.2435	0.1218
	d (MPa^{-1})	0.175	–			0.175	
Dilation angle (°)		1	1.5	2	3	1	0.5
Maximum shear dilation (μm)		35	52	70	105	35	18
Initial joint friction angle (°)		26.6					
Residual joint friction angle (°)		25					
Critical plastic shear strain		0.0002					

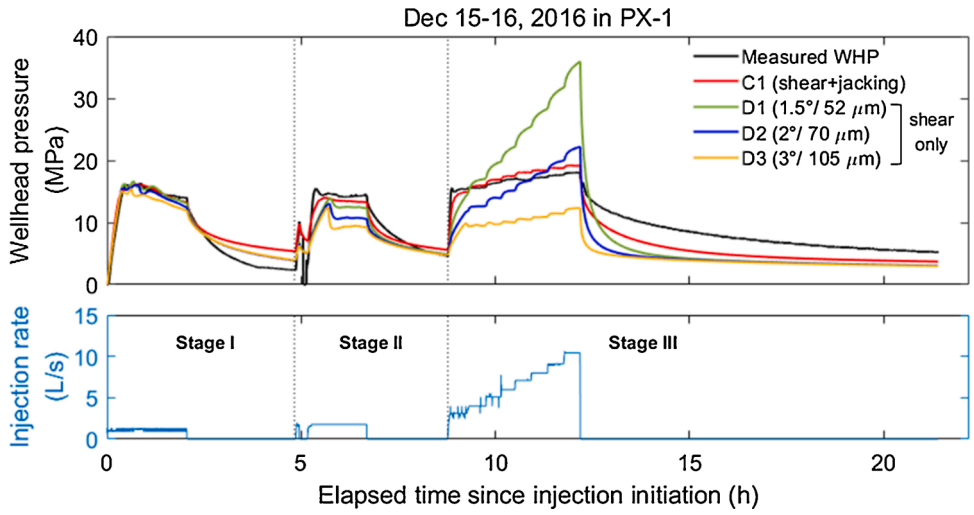

Fig. 14. Comparison of simulated wellhead pressure between models including only a shear slip and dilation component without jacking (D1, D2, and D3) and the reference model with combination of shear dilation and jacking (C1).

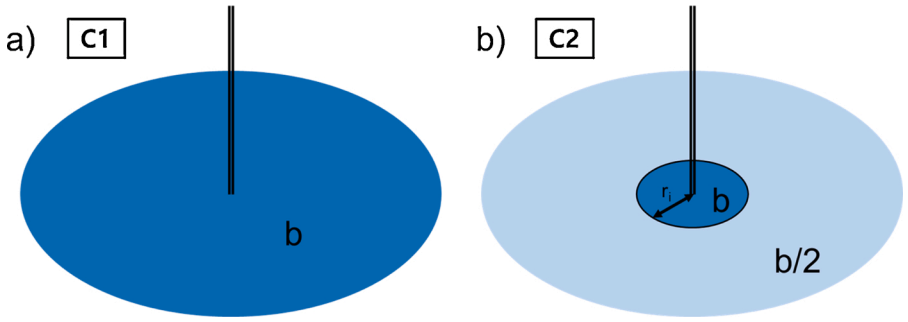

Fig. 15. Schematic diagram of equivalent aperture in the fracture zone in (a) C1 and (b) C2. In C2, further from a certain radial distance, r_i, from the injection element, the fracture zone had half of the residual hydraulic aperture (b_r), maximum deformation of the aperture (b_{max}), shear dilation angle, and maximum shear dilation.

Fitzgerald, 1998; Fjær et al., 2008; Zoback, 2010). In the PX-1 model of this study, the stress path coefficients were 0.42, 0.40, and 0.44 in the maximum, intermediate, and minimum principal stresses, respectively, at the onset of shear initiation. The shape of pressurized fracture zone elements was close to a cube of 10 m× 10 m× 10 m. Therefore, the ratios were comparable with the value estimated by Segall and Fitzgerald (1998) when the reservoir aspect ratio is 1. If the shape of fracture elements intersecting the well had been changed, the stress path coefficients would have been different resulting in a different critical pressure for shear slip. The uncertainly in the shape of the pressurized fracture zone volume at the very beginning of injection may add difficulty in the estimation of critical pressure for shear slip and the inverse estimation of the initial in-situ stress state from the wellhead pressure observation.

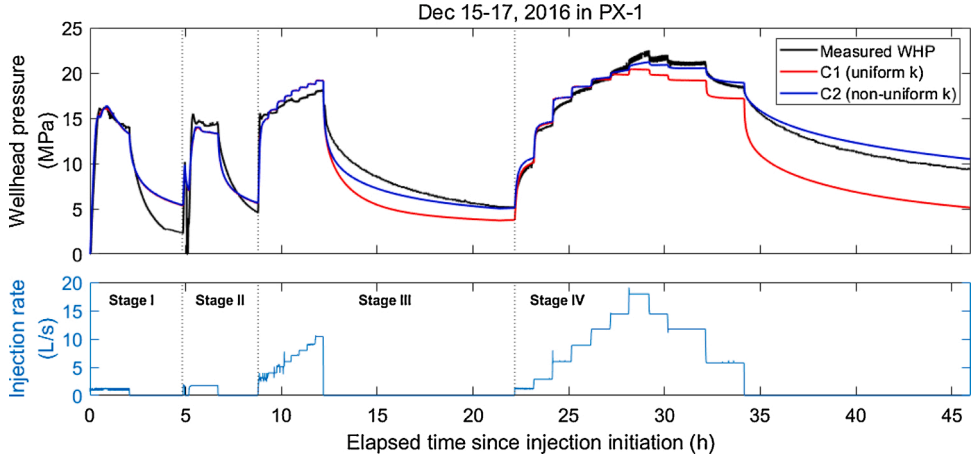

Fig. 16. Comparison of simulated wellhead pressure of the second hydraulic stimulation in two cases (C1 & C2).

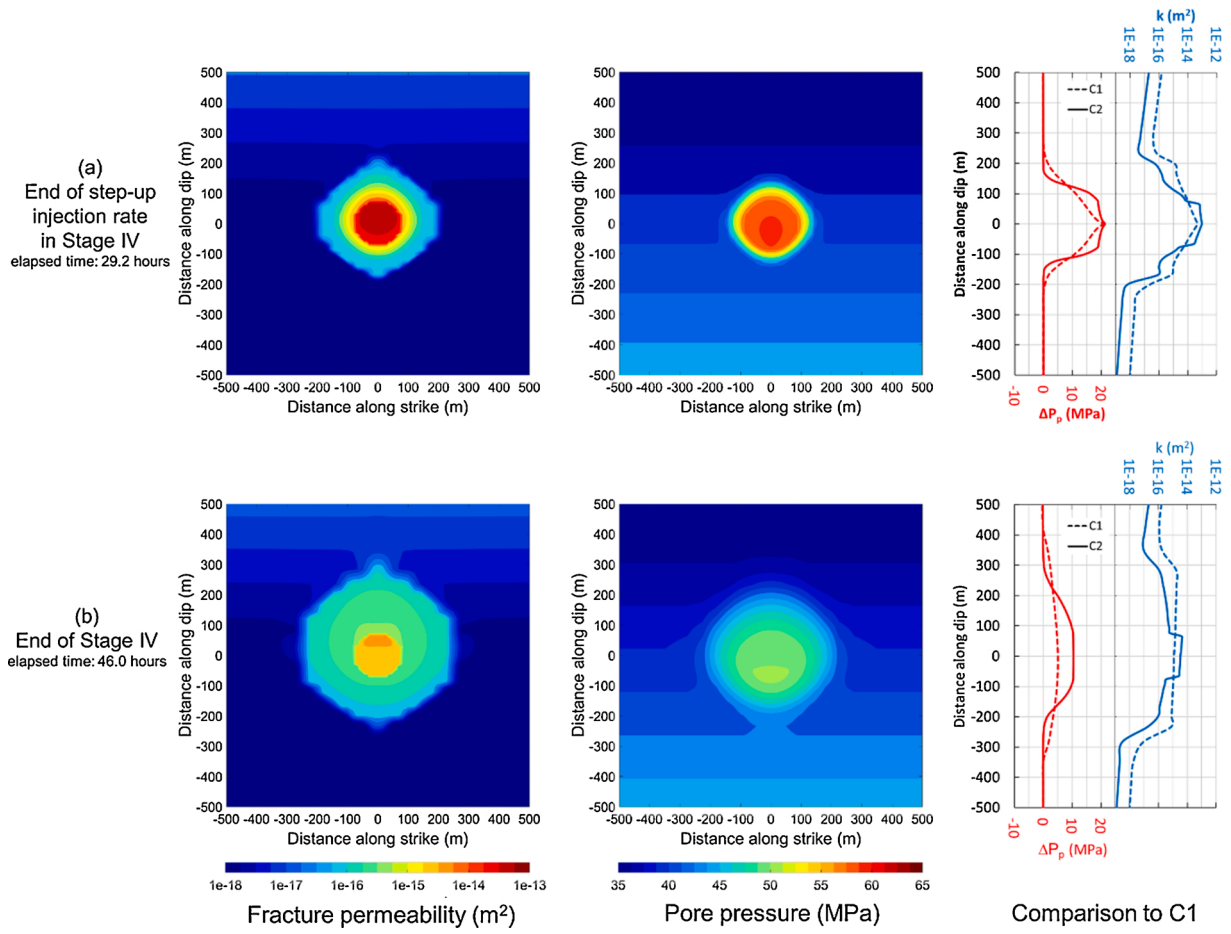

Fig. 17. Magnified contour diagrams of permeability and pore pressure on the fracture zone in C2 and comparisons of pore pressure change and permeability along the dip with the PX-1 reference model, C1. The center of each diagram is the intersection between the well and fracture zone.

4.2.4. *Alternative fracture zone models*

As a sensitivity study, two types of alternative models were set up as shown in Table 3. The first type (D1, D2, and D3) suppressed the hydraulic jacking of fracture with some increases in hydraulic shearing parameters such as dilation angle and maximum shear dilation. While the equivalent aperture in the reference model (C1) changed by both elastic opening and shear dilation, the first type models considered only shear dilation with a constant elastic residual aperture of 20 μm.

The simulated pressures from the first types (D1, D2, and D3) are compared with the reference model (C1) for the 22 h of Stages I-III in Fig. 14. Although all of the four models well reproduced the wellhead pressure in Stage I, differences were greater in the injection periods of Stages II and III. In D2 and D3, the fracture zone became too permeable and the wellhead pressure was underestimated in Stage II. The simulated pressure in D1 was higher than the measured pressure during the injection in Stage III. This indicates that shear dilation of a single dominant fracture alone cannot mimic the hydro-mechanical processes in the PX-1 fracture zone. In C1, the wellhead pressure was successfully reproduced by combining a shear dilation and hydraulic jacking in the fracture zone. Therefore, the simultaneous occurrence of shear slip and hydraulic jacking seems to be the key hydraulic stimulation mechanism for the reservoir near the PX-1 well.

The second type (C2) of the alternative model included an additional low permeable zone 75 m away from the injection well. In the lower permeability area of C2, key hydraulic inputs were half of those assigned for the reference model as shown in Table 3 and Fig. 15. In the reference model, simulated pressure began to be underestimated with the continued injection during the shut-in phase of Stage III and the step-down phase of Stage IV as shown in Fig. 8. This underestimated pressure indicates the possible presence of a zone with lower permeability away from the injection point.

The simulated pressures in C1 and C2 are compared with the observed pressure in Fig. 16. During the initial injections, both of the cases matched wellhead pressure equally well. However, C2 began to match better from the shut-in phase of Stage III, and a much better fit was achieved in Stage IV. This better fit at the later stage of injection strongly suggests the possible presence of zones with less permeability or even an impermeable barrier away from the injection point. In comparison to C1, C2 had more localized development of pressure and fracture permeability near the wellbore both after the step-up rate injection and shut-in in Stage IV (Fig. 17). In other words, an effective reservoir stimulation in PX-1 was likely spatially limited near the wellbore with the slow pressure diffusion. Recent studies show that the main fault of the 2017 Pohang M_w 5.5 earthquake is located a few hundred meters from the PX-1 boreholes (Lee, 2019; Woo et al., 2019), and there is a possibility that the injected fluid reached the impermeable fault core. Additional analysis may be required in this regard as a further study.

5. Conclusions

This study presents comprehensive coupled hydro-mechanical numerical modeling of the first and second hydraulic stimulations at the Pohang EGS site to improve the understanding on the key stimulation mechanisms in the fractured reservoir. Numerical modeling of the early days of each stimulation confirmed the candidate mechanisms of the fractured reservoir and significantly enhanced the understanding on the coupled behavior caused by the hydraulic stimulations. This study

demonstrates that the key hydro-mechanical processes of shear slip and dilation and hydraulic jacking observed in the fractured reservoir can be successfully reproduced in the numerical modeling.

Main conclusions are summarized as follows;

- Non-linear hydraulic jacking in the PX-2 hydraulic stimulation was confirmed through close history matching and comparison of simulated and observed aperture changes. Possible hydraulic fracturing or opening of pre-existing fractures observed in PX-2 was also found in the numerical modeling as the wellhead pressure stabilized around 67 MPa due to the use of exponential stress dependent permeability.
- Hydraulic shearing in the PX-1 hydraulic stimulation was successfully reproduced through the shear dilation and plastic strain softening model implemented in the fracture zone. The combined effect of shear dilation and hydraulic jacking was confirmed to be the main hydraulic stimulation mechanism in the reservoir near PX-1 borehole.
- Simulated critical wellhead pressure for shear slip near PX-1 well was greater than the prediction by a simple slip potential analysis in PX-1 due to local stress changes by the poroelastic effect. This shows that a coupled hydro-mechanical analysis is necessary for accurate estimation of critical pressure for shear slip and simple shear slip potential analyses may underestimate the critical wellhead pressure.
- Spatio-temporal changes in pressure, total stress, and permeability evaluated in the fracture zones greatly enhanced the understanding on the coupled behaviors in the fractured reservoir caused by the hydraulic stimulations. Considerable changes in total stress corresponding to the poroelastic effect and frictional-weakening shear slips have been found from the numerical investigation in the fracture zone.
- An alternative model with a lower permeable zone away from the injection well showed much better history matching after continued injection. This better fit at the later stage of injection strongly suggests the possible presence of zones with less permeability or even an impermeable barrier. Additional analysis may be required in this regard as a further study.

CRediT authorship contribution statement

Hwajung Yoo: Conceptualization, Methodology, Software, Investigation, Data curation, Writing - original draft, Writing - review & editing, Visualization. **Sehyeok Park:** Conceptualization, Methodology, Writing - review & editing, Visualization. **Linmao Xie:** Conceptualization, Writing - review & editing. **Kwang-Il Kim:** Conceptualization, Software, Writing - review & editing. **Ki-Bok Min:** Conceptualization, Methodology, Writing - original draft, Writing - review & editing, Supervision, Funding acquisition. **Jonny Rutqvist:** Methodology, Software, Writing - review & editing. **Antonio Pio Rinaldi:** Methodology, Software, Writing - review & editing.

Declaration of Competing Interest

The authors report no declarations of interest.

Acknowledgements

This work was supported by the Korea-EU Joint Research Support Program of the National Research Foundation of Korea (NRF) through a grant funded by the Korean Government's Ministry of Science, ICT and Future Planning (No. NRF-2015K1A3A7A03074226) as part of the EU DESTRESS project that has received funding from the European Union's Horizon 2020 research and innovation programme under grant agreement No. 691728. This work was also supported by the Korea Institute of Energy Technology Evaluation and Planning (KETEP) granted financial resources from the Ministry of Trade, Industry & Energy, Republic of Korea (No. 20123010110010). Additional funding was provided to J. Rutqvist by the U.S. Department of Energy under contract No. DE-AC02-05CH11231 to the Lawrence Berkeley National Laboratory. A. P. Rinaldi is currently funded by a SNSF Ambizione Energy grant (PZENP2_160555). The preparation of this manuscript was partially supported by the Institute of Engineering Research, Seoul National University. Additional funding was provided by a grant from the Human Resources Development program (No. 20204010600250) of the Korea Institute of Energy Technology Evaluation and Planning (KETEP), funded by the Ministry of Trade, Industry, and Energy of the Korean Government. We thank two anonymous reviewers for their constructive comments.

References

Baisch, S., Vörös, R., Rothert, E., Stang, H., Jung, R., Schellschmidt, R., 2010. A numerical model for fluid injection induced seismicity at Soultz-sous-Forêts. Int. J. Rock Mech. Min. Sci. 47 (3), 405–413.

Blöcher, G., Cacace, M., Jacquey, A.B., Zang, A., Heidbach, O., Hofmann, H., Kluge, C., Zimmermann, G., 2018. Evaluating micro-seismic events triggered by reservoir operations at the geothermal site of Groß Schönebeck (Germany). Rock Mech. Rock Eng. 51 (10), 3265–3279.

Cacace, M., Jacquey, A.B., 2017. Flexible parallel implicit modelling of coupled thermal–hydraulic–mechanical processes in fractured rocks. Solid Earth 8, 921–941.

Cappa, F., Rutqvist, J., 2011. Impact of CO2 geological sequestration on the nucleation of earthquakes. Geophys. Res. Lett. 38 (17).

Chang, K.W., Yoon, H., Kim, Y., Lee, M.Y., 2020. Operational and geological controls of coupled poroelastic stressing and pore-pressure accumulation along faults: induced earthquakes in Pohang, South Korea. Sci. Rep. 10 (1), 1–12.

Cheng, Q., Wang, X., Ghassemi, A., 2019. Numerical simulation of reservoir stimulation with reference to the Newberry EGS. Geothermics 77, 327–343.

Cladouhos, T., Petty, S., Larson, B., Iovenitti, J., Livesay, B., Baria, R., 2009. Toward more efficient heat mining: a planned enhanced geothermal system demonstration project. GRC Transactions 33, 165–170.

Dempsey, D., Kelkar, S., Davatzes, N., Hickman, S., Moos, D., 2015. Numerical modeling of injection, stress and permeability enhancement during shear stimulation at the Desert Peak enhanced Geothermal System. Int. J. Rock Mech. Min. Sci. 78, 190–206.

Diaz, M., Kim, K.Y., Yeom, S., Zhuang, L., Park, S., Min, K.-B., 2017. Surface roughness characterization of open and closed rock joints in deep cores using X-ray computed tomography. Int. J. Rock Mech. Min. Sci. 98, 10–19.

Economides, M.J., Nolte, K.G., 2000. Reservoir Stimulation, 3rd ed. John Wiley & Sons, New York.

Ellsworth, W.L., Giardini, D., Townend, J., Ge, S., Shimamoto, T., 2019. Triggering of the pohang, Korea, earthquake (M w 5.5) by enhanced geothermal system stimulation. Seismol. Res. Lett. 90 (5), 1844–1858.

Fjær, E., Holt, R.M., Raaen, A., Horsrud, P., 2008. Petroleum Related Rock Mechanics. Elsevier.

Hsiung, S.M., Chowdhury, A.H., Nataraja, M.S., 2005. Numerical simulation of thermal–mechanical processes observed at the Drift-Scale Heater Test at Yucca mountain, Nevada. USA. International Journal of Rock Mechanics and Mining Sciences 42 (5-6), 652–666.

Itasca, 2009. FLAC3D, Fast Lagrangian Analysis of Continua in 3 Dimensions, Version 4.0. Itasca Consulting Group, Minneapolis, Minnesota.

Jeanne, P., Rutqvist, J., Dobson, P.F., Walters, M., Hartline, C., Garcia, J., 2014. The impacts of mechanical stress transfers caused by hydromechanical and thermal processes on fault stability during hydraulic stimulation in a deep geothermal reservoir. Int. J. Rock Mech. Min. Sci. 72, 149–163.

Kamali, A., Ghassemi, A., 2018. Analysis of injection-induced shear slip and fracture propagation in geothermal reservoir stimulation. Geothermics 76, 93–105.

Kim, H., 2017. Integrated Estimation of In-situ Rock Stress at Pohang Geothermal Reservoir in Korea. PhD Dissertation. Seoul National University, South Korea.

Kim, K.-I., Min, K.-B., Kim, K.-Y., Choi, J.W., Yoon, K.-S., Yoon, W.S., Yoon, B., Lee, T.J., Song, Y., 2018. Protocol for induced microseismicity in the first enhanced geothermal systems project in Pohang, Korea. Renew. Sustain. Energy Rev. 91, 1182–1191.

Kohl, T., Hopkirk, R., 1995. "FRACure"—a simulation code for forced fluid flow and transport in fractured, porous rock. Geothermics 24 (3), 333–343.

Kohl, T., Mégel, T., 2007. Predictive modeling of reservoir response to hydraulic stimulations at the European EGS site Soultz-sous-Forêts. Int. J. Rock Mech. Min. Sci. 44 (8), 1118–1131.

Kolditz, O., Bauer, S., Bilke, L., Böttcher, N., Delfs, J.-O., Fischer, T., Görke, U.J., Kalbacher, T., Kosakowski, G., McDermott, C., 2012. OpenGeoSys: an open-source initiative for numerical simulation of thermo-hydro-mechanical/chemical (THM/C) processes in porous media. Environ. Earth Sci. 67 (2), 589–599.

Kwon, S., Xie, L., Park, S., Kim, K.-I., Min, K.-B., Kim, K.Y., Zhuang, L., Choi, J., Kim, H., Lee, T.J., 2019. Characterization of 4.2-km-deep fractured granodiorite cores from Pohang Geothermal Reservoir, Korea. Rock Mech. Rock Eng. 52 (3), 771–782.

Lee, K.-K., 2019. Final report of the korean government commission on relations between the 2017 pohang earthquake and EGS project. Geol. Soc. Korea.

Lee, T.J., Song, Y., Uchida, T., 2007. Three-dimensional magnetotelluric surveys for geothermal development in Pohang, Korea. Exploration Geophysics 38 (1), 89–97.

Lee, T.J., Song, Y., Yoon, W.S., Kim, K., Jeon, J., Min, K., Cho, Y., 2011. The first enhanced geothermal system project in Korea. Proceedings of the 9th Asian Geothermal Symposium 9.
Lee, T.J., Song, Y., Park, D.-W., Jeon, J., Yoon, W.S., 2015. Three dimensional geological model of Pohang EGS pilot site, Korea. Proceedings of the World Geothermal Congress, Melbourne, Australia.
Lim, H., Deng, K., Kim, Y.H., J.-H, R., Song, T.R.A., Kim, K.H., 2020. The 2017 Mw 5.5 Pohang earthquake, South Korea, and poroelastic stress changes associated with fluid injection. J. Geophys. Res. Solid Earth, e2019JB019134.
McClure, M.W., Horne, R.N., 2013. Discrete Fracture Network Modeling of Hydraulic Stimulation: Coupling Flow and Geomechanics. Springer Science & Business Media.
McClure, M.W., Horne, R.N., 2014. An investigation of stimulation mechanisms in enhanced Geothermal Systems. Int. J. Rock Mech. Min. Sci. 72, 242–260.
Min, K.-B., Rutqvist, J., Tsang, C.-F., Jing, L., 2004. Stress-dependent permeability of fractured rock masses: a numerical study. Int. J. Rock Mech. Min. Sci. 41 (7), 1191–1210.
Norbeck, J.H., McClure, M.W., Horne, R.N., 2018. Field observations at the Fenton Hill enhanced geothermal system test site support mixed-mechanism stimulation. Geothermics 74, 135–149.
Park, S., Xie, L., Kim, K.-I., Kwon, S., Min, K.-B., Choi, J., Yoon, W.-S., Song, Y., 2017. First hydraulic stimulation in fractured geothermal reservoir in pohang PX-2 well. Procedia Eng. 191, 829–837.
Park, S., Kim, K.-I., Xie, L., Yoo, H., Min, K.-B., Kim, M., Yoon, B., Kim, K.Y., Zimmermann, G., Guinot, F., 2020. Observations and analyses of the first two hydraulic stimulations in the Pohang geothermal development site, South Korea. Geothermics 88, 101905.
Pine, R., Batchelor, A., 1984. Downward migration of shearing in jointed rock during hydraulic injections. International Journal of Rock Mechanics and Mining Sciences & Geomechanics Abstracts. Elsevier, pp. 249–263.
Pruess, K., Oldenburg, C., Moridis, G., 2012. TOUGH2 User's Guide, Version 2.1, LBNL-43134 (revised). Lawrence Berkeley National Laboratory, Berkeley, CA.
Rinaldi, A.P., Rutqvist, J., 2019. Joint opening or hydroshearing? Analyzing a fracture zone stimulation at Fenton Hill. Geothermics 77, 83–98.
Rinaldi, A.P., Rutqvist, J., Cappa, F., 2014. Geomechanical effects on CO2 leakage through fault zones during large-scale underground injection. Int. J. Greenh. Gas Control. 20, 117–131.
Rinaldi, A.P., Rutqvist, J., Sonnenthal, E.L., Cladouhos, T.T., 2015. Coupled THM modeling of hydroshearing stimulation in tight fractured volcanic rock. Transp. Porous Media 108 (1), 131–150.
Rutqvist, J., 2017. An overview of TOUGH-based geomechanics models. Comput. Geosci. 108, 56–63.
Rutqvist, J., Stephansson, O., 1996. A cyclic hydraulic jacking test to determine the in situ stress normal to a fracture. International Journal of Rock Mechanics and Mining Sciences & Geomechanics Abstracts. Elsevier, pp. 695–711.
Rutqvist, J., Tsang, C.-F., 2003. Analysis of thermal–hydrologic–mechanical behavior near an emplacement drift at Yucca mountain. J. Contam. Hydrol. 62-63, 637–652.
Rutqvist, J., Rinaldi, A.P., Cappa, F., Moridis, G.J., 2015. Modeling of fault activation and seismicity by injection directly into a fault zone associated with hydraulic fracturing of shale-gas reservoirs. J. Pet. Sci. Eng. 127, 377–386.
Rutqvist, J., Figueiredo, B., Hu, M., Tsang, C.-F., 2018. Continuum modeling of hydraulic fracturing in complex fractured rock masses. Hydraulic Fracture Modeling. Elsevier, pp. 195–217.
Segall, P., Fitzgerald, S.D., 1998. A note on induced stress changes in hydrocarbon and geothermal reservoirs. Tectonophysics 289 (1-3), 117–128.
Vilarrasa, V., Rinaldi, A.P., Rutqvist, J., 2017. Long-term thermal effects on injectivity evolution during CO2 storage. Int. J. Greenh. Gas Control. 64, 314–322.
Witherspoon, P.A., Wang, J.S., Iwai, K., Gale, J.E., 1980. Validity of cubic law for fluid flow in a deformable rock fracture. Water Resour. Res. 16 (6), 1016–1024.
Woo, J.U., Kim, M., Sheen, D.H., Kang, T.S., Rhie, J., Grigoli, F., Ellsworth, W., Giardini, D., 2019. An in-depth seismological analysis revealing a causal link between the 2017 MW 5.5 Pohang earthquake and EGS project. J. Geophys. Res. Solid Earth 124 (12), 13060–13078.
Yeo, I.W., Brown, M.R.M., Ge, S., Lee, K.K., 2020. Causal mechanism of injection-induced earthquakes through the Mw 5.5 Pohang earthquake case study. Nat. Commun. 11 (1), 2614.
Yin, Z., Huang, H., Zhang, F., Zhang, L., Maxwell, S., 2020. Three-dimensional distinct element modeling of fault reactivation and induced seismicity due to hydraulic fracturing injection and backflow. Joumal Rock Mech. Geotech. Eng. 12 (4), 752–767.
Yoo, H., 2018. Numerical Modeling of Hydraulic Stimulation at a Fractured Geothermal Reservoir. Master's Thesis. Seoul National University, South Korea.
Yoon, K., Jeon, J., Hong, H., Kim, H., Hakan, A., Park, J., Yoon, W., 2015. Deep drilling experience for Pohang enhanced geothermal project in Korea. In: Proceedings of the World Geothermal Congress. Melbourne, Australia.
Zbinden, D., Rinaldi, A.P., Urpi, L., Wiemer, S., 2017. On the physics-based processes behind production-induced seismicity in natural gas fields. J. Geophys. Res. Solid Earth 122 (5), 3792–3812.
Zoback, M.D., 2010. Reservoir Geomechanics. Cambridge University Press.